mathematics

MDPI

*Article*

# A Spectral Framework for Identifying Frequency-Dependent Instrumental Sensitivity

**Miroslava Jordovic Pavlovic [1,*], Slobodanka Galovic [2], Dalibor Chevizovich [2], Edin Suljovrujic [2], Dejan Milicevic [2], Katarina Djordjevic [2] and Marica N. Popovic [3,*]**

[1] Faculty of Mechanical and Civil Engineering in Kraljevo, University of Kragujevac, Dositejeva 19, 36000 Kraljevo, Serbia
[2] Vinca Institute of Nuclear Sciences, University of Belgrade, 11351 Belgrade, Serbia; bobagal@vin.bg.ac.rs (S.G.); cevizd@vin.bg.ac.rs (D.C.); edin@vin.bg.ac.rs (E.S.); dejanmilicevic@vin.bg.ac.rs (D.M.); katarina.djordjevic@vin.bg.ac.rs (K.D.)
[3] Institute of Physics Belgrade, University of Belgrade, Pregrevica 118, 11080 Belgrade, Serbia
* Correspondence: jordovicpavlovic.m@mfkv.kg.ac.rs (M.J.P.); marica.popovic@ipb.ac.rs (M.N.P.)

**Abstract**

Measured signals are shaped not only by the physical system under investigation but also by the measurement apparatus, whose transfer characteristics are often only approximately known and unevenly distributed over the spectrum. This paper develops a mathematical framework for identifying where a measured signal is most sensitive to an unknown measurement response. The instrument is described by a family of real rational transfer functions with known structural form but uncertain parameters. For a fixed reference signal, the admissible measured-signal ensemble's covariance matrix is formed and eigendecomposed; its dominant directions of instrument-induced variability, projected onto the frequency axis, give a frequency-resolved map of instrumental sensitivity. The framework is diagnostic: it does not estimate the instrument's parameters, reduce the physical signal, or solve an inverse problem, and its integration into inverse analysis is left for future work. The approach is illustrated on simulated photoacoustic signals for three microphone classes. Seven dominant modes explain 98.8% of the variance and reveal a narrow, low-redundancy spectral band, which overlaps the regions that a supervised correlation analysis of the 400-dimensional representation identifies as informative for some instrument parameters. A previously validated regression model recovers the instrument parameters with 97.27% accuracy from seven features selected by this analysis (98.84% from all 400).

**Keywords:** photoacoustic; measurement operator; instrumental sensitivity; microphone; inverse problems

**MSC:** 65J22; 62H25; 94A12

Check for updates

Academic Editors: Zulima Fernández-Muñiz and Juan Luis Fernández-Martínez

Received: 7 October 2026
Revised: 8 November 2026
Accepted: 16 November 2026
Published: 18 November 2026

**Copyright:** © 2026 by the authors. Licensee MDPI, Basel, Switzerland. This article is an open access article distributed under the terms and conditions of the Creative Commons Attribution (CC BY) license.

## 1. Introduction

In experimental measurements, the observed signal results from the action of both the physical system under investigation and the measurement system itself. The recorded signal, therefore, in general, does not represent a direct image of the physical response; it is shaped by the transfer characteristics of the detector, the electronics, and other elements of the measurement apparatus. This influence can be particularly significant in the frequency domain, where certain frequency regions may be considerably more sensitive to the characteristics of the measurement system than others.

Common approaches to correcting the instrumental influence most often require prior knowledge or calibration of the frequency response of the particular measurement system [1], or its identification from data [2–4]. In general, however, such a response is not necessarily known with sufficient accuracy. In addition, replacing the detector or other elements of the measurement apparatus may change the transfer characteristic of the system, so that a predefined frequency region of unreliable measurement cannot be considered universal. Even the poles and zeros of the instrumental transfer function that lie outside the directly observed frequency range may influence the response within it.

The consequences are particularly serious in inverse problems [5,6], which are typically ill-posed and require regularization and careful treatment of measurement uncertainty [7,8]. Inverse problems with imperfect forward operators have therefore received considerable attention in regularization theory, where uncertainties in the operator are explicitly incorporated into the reconstruction procedure [9,10].

In this work, we consider instrumental influence in a general form, through a class of real rational transfer functions whose structure is known, while their parameters, including the positions of poles and zeros, need not be determined precisely in advance. Instead of first attempting to identify such a response explicitly, we consider the set of possible measurement responses corresponding to admissible variations of the instrumental parameters. This makes it possible to examine how the uncertainty of the instrumental response affects different components of the measured signal.

The main goal is not to discard a certain part of the frequency spectrum in advance, as in truncation-based regularization [11], nor to reduce the measured signal to a small number of components. The goal is to identify those frequency regions in which the measurement is particularly sensitive to the unknown instrumental response. The dominant variations caused by changes in the instrumental parameters determine an instrumental-sensitivity subspace, whose projection onto the frequency axis provides information on where the influence of the measurement apparatus is greatest. In this way, parts of the spectrum with different degrees of sensitivity to instrumental uncertainty can be distinguished.

The approach is related in spirit to methods that exploit the low-dimensional structure of inverse problems, such as likelihood-informed subspaces of the parameter space [12,13] and optimal low-rank approximations of the posterior distribution [14]. Principal component analysis of model outputs has likewise been used to reduce high-dimensional outputs for sensitivity analysis [15] and to identify the dominant collective variations that propagate structural uncertainty into calculated spectra [16]. The problem considered here is, however, different: rather than seeking informative directions in the parameter space, we examine the structure that an uncertain measurement operator induces in the measurement space itself.

The information obtained is a result of measurement preprocessing and is intended for use in the subsequent stage of analysis. Frequency regions with pronounced instrumental sensitivity may, depending on the particular inverse problem, be excluded from the analysis, weighted differently, or assigned a larger measurement uncertainty. Conversely, regions in which the influence of the instrumental parameters is weaker may be used with a lower degree of instrumental uncertainty. In this way, the strategy for solving the inverse problem is not defined in advance but can be adapted on the basis of the previously established frequency distribution of instrumental sensitivity.

The proposed approach therefore does not replace the physical model of the system nor the solution of the inverse problem itself. Its role is to provide, before physical interpretation and inverse identification, information on where the measurement result is most sensitive to the unknown instrumental response. The instrumental influence is thus included in the organization of the inverse analysis already at the preprocessing level, without the need

to assume in advance that a single, fixed frequency region is necessarily unreliable for all realizations of the measurement system.

This problem is particularly relevant in photoacoustic (PA) measurements, where the registered signal arises from a complex interaction of the physical response of the system and the characteristics of the measurement chain, including the microphone and electronic acquisition [1]. Quantitative PA reconstruction is naturally formulated as an inverse problem [17,18], and model mismatch has been shown to affect the reconstructed quantities substantially [19]. The PA system therefore represents a suitable case study for demonstrating the proposed approach: instead of a prescribed selection of the frequency range, the regions in which the registered signal is most sensitive to unknown instrumental parameters are identified first, and this information can then be used for an appropriate formulation of the subsequent inverse analysis.

We state at the outset what this paper does and does not claim. Its contribution is a diagnostic method: it localizes the frequency regions in which the measured signal is most sensitive to uncertainty of the instrumental response, using the covariance structure of an ensemble of measured signals generated by admissible variations of the instrument parameters. It is not an inverse-problem solver, and we make no claim that excluding or down-weighting the identified regions improves a particular inversion algorithm; that question is the subject of separate work. The motivation is the uncertainty of the filtering properties of the measurement chain, of which the microphone is a concrete example: such uncertainty may make some frequencies sensitive, but this is not a sufficient reason to discard them automatically, since they may also carry information about the sample. The map shows where the registered spectrum changes under admissible variations of the instrument parameters, so that the problem becomes visible before it is decided how the spectrum is used; it does not by itself reconstruct the actual transfer response and does not prescribe the rejection of flagged frequencies.

The individual tools are standard. Covariance eigendecomposition, truncation to the $k$ dominant modes and the diagonal of the truncated covariance matrix belong to principal component analysis [20,21]; in particular, the quantity $S_{\text{inst}}$ defined in Section 2.5 is the diagonal of the rank-$k$ approximation of the correlation matrix, known in PCA as the communality of a variable, and the correlation analysis of Section 3.2.3 is conventional. PCA-based sensitivity analyses of model outputs [15,16] use the principal components of an output ensemble to compress high-dimensional outputs and to attribute their variability to uncertain inputs or to structural uncertainty of the model of the observed system. Here the uncertain object is instead the measurement operator acting on a fixed reference signal, and the quantity of interest is the distribution of the operator-induced variability over the frequency axis, not a ranking of input parameters. The contribution of the paper is therefore not a new statistical tool but (i) the formulation of the instrument as a family of multiplication operators with a structurally known transfer function, whose admissible variations generate the ensemble; (ii) the interpretation of the diagonal of the truncated covariance as a frequency-resolved map of instrumental sensitivity, together with the explicit limits of that interpretation (Remark 1); and (iii) the relation, in a photoacoustic case study, between this unsupervised map and a supervised correlation-based selection of the features used for the regression-based identification of the instrument parameters; the two answer different questions and are complementary.

The remainder of the paper is organized as follows. Section 2 develops the theoretical framework, Section 3 presents the PA case study, and Section 4 summarizes the conclusions.

## 2. Theoretical Framework

For a family of admissible instrumental responses and a fixed reference signal, we form the set of possible measured signals. Analysis of the covariance of this set identifies the dominant directions of variation caused by the instrumental parameters, and the projection of these directions onto the frequency domain determines the regions in which the measurement is most sensitive to instrumental uncertainty. The construction is developed in Sections 2.1–2.5, and Section 2.6 discusses how its outcome can enter an inverse analysis.

### *2.1. Measurement Operator*

Let $\omega$ denote the angular frequency ($f = \omega/2\pi$), $x(\omega)$ the ideal (physical) signal, and $y(\omega)$ the measured signal. The measurement is modeled as

$$y(\omega) = M(\omega;\theta)\, x(\omega), \tag{1}$$

where $M(\omega;\theta)$ is the instrumental measurement operator and $\theta$ is the vector of unknown instrumental parameters. For a linear time-invariant measurement system, the measured signal in the time domain is the convolution of the ideal signal with the impulse response of the system, which corresponds to multiplication by the transfer function $T(\omega;\theta)$ in the frequency domain; $M(\omega;\theta)$ is then the associated multiplication operator. That the observation operator is not merely a passive detail of an inverse problem, and that its choice and mismatch with the true one affect the resulting inference, has been analyzed in [22].

We assume that the structure of the class of operators is known: $T$ is a real rational function,

$$T(\omega;\theta) = \frac{\sum_{m=0}^{q} b_m\,(j\omega)^m}{\sum_{n=0}^{p} a_n\,(j\omega)^n}, \tag{2}$$

with real coefficients $a_n$ and $b_m$ collected in $\theta$ (equivalently, $T$ is determined by the positions of its poles and zeros and a gain), whereas the concrete parameter values are not known in advance. In particular, poles and zeros lying outside the directly observed frequency range may still influence the response within it. On a frequency grid $\omega_1, \ldots, \omega_N$, the signals are represented by vectors $x, y \in H = \mathbb{C}^N$ and $(M(\theta)x)_n = T(\omega_n;\theta)\, x_n$.

The model (1) and the construction below rest on three assumptions that delimit their domain of applicability. (i) Linearity: $T$ does not depend on the signal level, which holds while the detector operates in its linear range; nonlinear distortion in the measurement chain is not covered. (ii) Time invariance: $T$ is constant during the acquisition of a spectrum, so slow drifts of the instrument parameters are not represented. (iii) Noise: the ensemble (4) is generated without additive noise, $y = M(\theta)x$; measurement noise, which does not originate in the operator, would add a contribution to $\Sigma$ that is unrelated to $\theta$. These effects are not modelled in the simulated data of Section 3, and how they alter the sensitivity map is outside the scope of this paper; the robustness of the regression probe used in Section 3 to random noise of $\pm 5\%$ is discussed in Section 3.2.3.

### *2.2. Admissible Family of Measurement Operators*

Let $\Theta \subset \mathbb{R}^d$ be the set of admissible parameter values (for example, prescribed ranges of the individual parameters), where $d$ is the number of instrumental parameters. The admissible family of measurement operators is

$$\mathcal{M} = \{M(\omega;\theta) : \theta \in \Theta\}. \tag{3}$$

For a fixed reference signal $x$, the corresponding set of possible measured signals is

$$y_i = M(\theta_i)\, x, \qquad \theta_i \in \Theta, \quad i = 1, \ldots, K. \tag{4}$$

We therefore do not attempt to identify the actual operator $M$; instead, we examine how much the possible measurements change within the admissible class of instrumental responses [23].

In practice, the set $\Theta$ may be specified from manufacturer specifications, from calibration measurements, from a prior model of the instrument or from expert judgment; whichever source is used must be stated, because the sensitivity map depends on $\Theta$. The ranges used in the case study and their source are given in Section 3.2.1.

### 2.3. Instrument-Induced Variability

The ensemble in Equation (4) is centered and its covariance matrix is formed,

$$\bar{y} = \frac{1}{K}\sum_{i=1}^{K} y_i, \qquad \Sigma = \frac{1}{K}\sum_{i=1}^{K}(y_i - \bar{y})(y_i - \bar{y})^H, \tag{5}$$

where $(\cdot)^H$ denotes the conjugate transpose. The matrix $\Sigma$ is Hermitian and positive semidefinite (real symmetric if a real-valued amplitude–phase representation of the spectrum is used). In practice, the components of $y_i$ span several orders of magnitude across the frequency grid (Section 3.2), so each component is first standardized to zero mean and unit variance before $\Sigma$ is formed; $\Sigma$ is then the correlation matrix of the ensemble, and its diagonal entries no longer carry the absolute scale of the measured quantity. Its eigendecomposition

$$\Sigma v_j = \lambda_j v_j, \qquad \lambda_1 \geq \lambda_2 \geq \cdots \geq \lambda_N \geq 0, \tag{6}$$

with orthonormal eigenvectors $v_j$, is the principal component analysis of the ensemble [20,21]. Large eigenvalues identify directions in the measurement space along which the measured signal is most sensitive to admissible variations of the instrumental response, whereas directions associated with small eigenvalues are only weakly affected. The matrix $\Sigma$ characterizes the variability caused by the instrument for the given reference signal; it does not by itself make any statement about the physical information contained in $x$.

Standardization is more than a numerical convenience: it changes the meaning of the resulting map and is therefore stated explicitly. With the raw covariance matrix, large diagonal elements mark the frequencies at which the operator induces the largest absolute variance, so the result is governed by the few components of highest variance; with the correlation matrix, every component has unit variance, and $S_{\text{inst}} \in [0, 1]$ measures how completely the dominant modes reproduce each frequency, irrespective of its scale. In the case study, the variances of the amplitude features span more than nine orders of magnitude (from $5.4 \times 10^{-10}$ to 5.1), and those of the phase features run from 0.16 to $1.9 \times 10^{3}$ in the units of the database, so the raw covariance would compare components of incommensurate scales. A direct comparison of the two variants is given in Section 3.2.5.

### 2.4. Dominant Instrument-Sensitivity Subspace

The dominant instrument-sensitivity subspace is spanned by the leading eigenvectors,

$$S_k = span\{v_1, \ldots, v_k\}, \tag{7}$$

and the fraction of the instrument-induced variability captured by its first $k$ modes is measured by

$$\eta_k = \frac{\sum_{j=1}^{k} \lambda_j}{\sum_{j=1}^{N} \lambda_j}. \tag{8}$$

The number of modes $k$ is chosen according to a stated criterion, for example as the smallest $k$ for which $\eta_k$ exceeds a prescribed threshold [24]. It is therefore a result of the analysis of the variability structure. It is not assumed to be equal to the number $d$ of

instrumental parameters, and it is not imposed by the number $N$ of frequency samples. The subspace $S_k$ describes instrumental sensitivity; it is not claimed to contain, or to exclude, information about the physical system.

Because the threshold on $\eta_k$ is a modelling choice, no single value is treated as canonical; the dependence of the results on $k$ and on the threshold is reported in Sections 3.2.2 and 3.2.5.

**Remark 1.** *Retaining k modes means only that the first k eigenmodes capture the dominant part of the instrument-induced variability according to the chosen criterion. This is an approximation and not an exact confinement of all variations to $S_k$. Accordingly, the complement of $S_k$ is not claimed to be invariant with respect to the instrument, and no claim is made that the components outside $S_k$ either preserve or must be discarded with respect to the physical signal. Moreover, the eigenvectors $v_j$ are directions in a space of dimension N; k dominant eigenvectors do not in general correspond to k individual frequencies.*

### *2.5. Frequency-Resolved Instrumental Sensitivity*

The abstract instrument-sensitivity subspace is now returned to the original frequency representation. Let $v_j(\omega_n)$ denote the component of the eigenvector $v_j$ at frequency $\omega_n$. The frequency-resolved instrumental sensitivity is defined as

$$S_{inst}(\omega_n) = \sum_{j=1}^{k} \lambda_j \left| v_j(\omega_n) \right|^2, \tag{9}$$

that is, the $n$-th diagonal element of the rank-$k$ approximation $\Sigma_k = \sum_{j=1}^{k} \lambda_j v_j v_j^H$ of the covariance matrix. It is the part of the variance of the measured signal at frequency $\omega_n$, caused by admissible instrumental variations, that is captured by the dominant modes. If the measured spectrum is represented by amplitude and phase, the map is obtained separately for the amplitude and phase components. When $\Sigma$ is computed from the raw (unnormalized) ensemble, large values of $S_{\text{inst}}$ mark spectral regions where the absolute variance induced by the instrument is largest. When, as in practice, $\Sigma$ is the correlation matrix of the standardized ensemble, every frequency has unit variance by construction, and $S_{\text{inst}}(\omega_n) \in [0, 1]$ instead measures how completely the $k$ dominant, instrument-shared modes reconstruct that particular frequency: values close to 1 indicate that the frequency's variability is redundant with the bulk of the spectrum, while a reduced value marks a frequency whose instrument-induced variability is comparatively independent of the dominant modes and therefore requires additional modes, beyond the first $k$, to be fully resolved.

**Remark 2.** *For the correlation matrix, $S_{inst}(\omega_n)$ in Equation (9) equals the squared multiple correlation of the n-th standardized component with the first k principal components, that is, the fraction of its variance explained by them (the communality of the component in PCA). Equation (9) is therefore an established PCA identity; what is specific here is its interpretation as a frequency-resolved map of the sensitivity of the measured spectrum to uncertainty in the measurement operator, and the claims made in this paper are limited to that interpretation.*

Operationally, a frequency $\omega_n$ is flagged as instrument-sensitive if $S_{\text{inst}}(\omega_n) < \tau$, where $\tau \in (0,1)$ is a threshold chosen by the user, and amplitude and phase components are flagged separately. The condition $S_{\text{inst}} < \tau$ means that more than the fraction $1 - \tau$ of the standardized variance at $\omega_n$ is not reproduced by the $k$ dominant modes. In the case study we use $\tau = 0.9$; Section 3.2.5 reports the dependence on $\tau$ and on $k$. The choice of $\tau$ is not arbitrary. Because $S_{\text{inst}}(\omega_n)$ does not decrease with $k$, the flagged sets are nested in $k$ (Supplementary Materials, Section S1). A threshold can also be related to the experimental tolerance $\varepsilon$: if the part of the response not reproduced by the $k$ dominant modes is what

matters, a frequency is flagged when $\sigma_n\sqrt{1 - S_{inst}(\omega_n)} > \varepsilon$, where $\sigma_n$ is the ensemble standard deviation of the component at $\omega_n$, i.e., when $S_{inst}(\omega_n) < \tau_n = 1 - \left(\frac{\varepsilon}{\sigma_n}\right)^2$. For $\varepsilon$ equal to 5% of the amplitude, the band obtained in this way contains the band for $\tau = 0.9$ and extends it by one to three indices on each side (Section S2). We do not claim a unique optimal value of $\tau$. The criterion makes the identification reproducible, but $\tau$ remains a modelling choice, like the threshold on $\eta_k$. $S_{\mathrm{inst}}(\omega_{\mathrm{n}})$ is therefore a relative measure, namely the fraction of the standardized variance at $\omega_{\mathrm{n}}$ that the $k$ dominant modes reproduce; it is not a measure of the absolute distortion of the signal and not an automatic criterion for rejecting a frequency.

The construction thus follows the chain:

admissible instrumental variations → dominant modes → frequency-resolved sensitivity.

In the case study of Section 3 the map is computed from the simulated ensemble; separately, a supervised correlation analysis identifies the spectral samples that carry information on the instrument parameters and is used to select a small number of features. The two are complementary and are related in Section 3.2.4.

### *2.6. Implications for Inverse Analysis*

Only at this point, as the last step, do we indicate what the obtained map is used for. The map $S_{\mathrm{inst}}(\omega)$ provides information that can subsequently be incorporated into the formulation of an inverse problem in several ways, for example through:

- exclusion of strongly instrument-sensitive regions;
- frequency-dependent weighting;
- uncertainty weighting;
- robust inversion;
- joint estimation of physical and instrumental parameters.

The proposed method does not choose among these strategies; that is the subject of separate research, which follows naturally from this work but is not part of it. The choice depends on the forward theoretical problem and on the characteristics of the measured sample, that is, on whether a given spectral region contains information that is masked by the instrumental influence, amplified by it, or needed but not indispensable and, being strongly modified by the instrumental influence, capable of reducing the accuracy of the solution of the inverse problem.

The sensitivity map should therefore be understood as a diagnostic instrument and not as a preprocessing step with a guaranteed effect on inversion. No inverse problem is solved in this paper, and we make no claim that excluding or down-weighting the flagged regions improves a specific inversion algorithm; the integration of the map into inverse solvers is future work.

## 3. Case Study: Photoacoustic Measurement

### *3.1. Photoacoustic Measurement Model*

Photoacoustic (PA) measurements are used here solely as a representative example of a measurement system in which the detector introduces a structured, frequency-dependent operator whose influence can be analyzed within the proposed framework. PA measurement methods presented in this research are based on the conversion of periodically modulated optical energy into acoustic waves. When a sample is illuminated by an optical beam with periodic intensity modulation, the absorbed energy produces time-varying temperature fields inside the material. These temperature variations, in turn, induce pressure fluctuations that can be detected as an acoustic signal [25–30].

In gas–microphone PA configurations, typically realized using a small, closed transmission cell, the optical excitation and the microphone are positioned on opposite sides of the sample. In this geometry, the cavity in front of the microphone diaphragm forms the effective acoustic volume in which the pressure oscillations are generated [31,32]. The periodic nature of the excitation ensures that the resulting PA response can be represented as harmonic components at known modulation frequencies. This arrangement naturally leads to a frequency-domain formulation of the measurement process and justifies modeling the detector influence through a frequency-dependent transfer operator $M$ acting on the ideal pressure response [33,34].

From the physical point of view, two principal mechanisms contribute to the generation of the PA signal. The first is the thermal piston mechanism, governed by the propagation of heat waves in the material and its surroundings. This is a dissipative process controlled by the thermal conductivity, diffusivity, and related transport parameters. The second mechanism is thermoelastic expansion, in which thermal energy is directly coupled to the vibration modes of the solid. This process is essentially non-dissipative and propagates with the speed of sound through the sample. The total PA pressure can therefore be viewed as the superposition of the thermoconducting and the thermoelastic components, each with its own characteristic dependence on frequency and material properties [30,31,33,34]. Based on the developed theoretical–mathematical model for the total PA signal recorded by a minimal-volume PA cell experimental setup, $\tilde{p}_{tot}$ and $S(f)$ are given by:

$$\tilde{p}_{tot} = \tilde{p}_{th} + \tilde{p}_{ac} \tag{10}$$

$$\tilde{p}_{th} = \frac{\gamma P_0}{l_g T_0} \frac{\sqrt{D_{Tg}}}{\sqrt{j\omega\left(1 + j\omega\tau_g\right)}} \tilde{\vartheta}(l_s) \tag{11}$$

$$\tilde{p}_{ac} = \frac{3\gamma P_0}{l_a} a_T \frac{R^2}{l_s^3} \int_0^{l_s} \left(x - \frac{l_s}{2}\right) \tilde{v}_s(x)\, dx \tag{12}$$

$$T(f) = \frac{1}{1 - j\frac{f_2}{f}} \left( \frac{f_3^2}{f_3^2 - f^2 + jff_3\xi_3} + \frac{f_4^2}{f_4^2 - f^2 + jff_4\xi_4} \right) \tag{13}$$

$$S(f) = \tilde{p}_{tot}(f)\, T(f) \tag{14}$$

Here, $\tilde{p}_{tot}$ [Pa] denotes the total pressure recorded by the PA setup, while $\tilde{p}_{th}$ [Pa] and $\tilde{p}_{ac}$ [Pa] represent the thermoconductive and thermoelastic components, respectively. $P_0$ [Pa] denotes the cell pressure, $\gamma$ is the heat capacity ratio, and $a_T$ [$K^{-1}$] is the thermal expansion coefficient. The symbols $R$ [m] and $l_g$ [m] represent the radius and length of the chamber in front of the microphone diaphragm, respectively, while $l_s$ [m] denotes the thickness of these two layers. In the case of a very thin coating, this thickness can be approximated by the thickness of the investigated sample. Finally, $\tilde{v}_s(x)$ [K] denotes the temperature variation inside the sample, while $\tilde{\vartheta}(l_s)$ [K] represents the surface temperature variation at the rear surface.

In terms of Section 2, Equations (10)–(12) give the PA pressure $\tilde{p}_{\mathrm{tot}}(f)$ generated by the sample, which plays the role of the ideal signal $x$ in Equation (1). Equation (13) is the transfer function $T(f)$ of the detector chain (dimensionless), parameterized by $\theta = (f_2, f_3, f_4, \xi_3, \xi_4)$: $f_2$ [Hz] is the characteristic frequency of the high-pass (RC) part, $f_3$ and $f_4$ [Hz] are the two acoustic resonance frequencies of the microphone, and $\xi_3$ and $\xi_4$ are the corresponding dimensionless damping coefficients (reciprocal quality factors) [1]. Equation (14) states that the measured signal $S(f)$ is the product of the ideal pressure and $T(f)$, that is, $y = M(\theta)x$ with $x = \tilde{p}_{\mathrm{tot}}$ and $y = S$; additive noise is not included, in accordance with the assumptions of Section 2.1.

The frequency-dependent amplitude and phase characteristics of a representative detector transfer function are illustrated in Figure 1, together with the ideal flat response used as a reference.

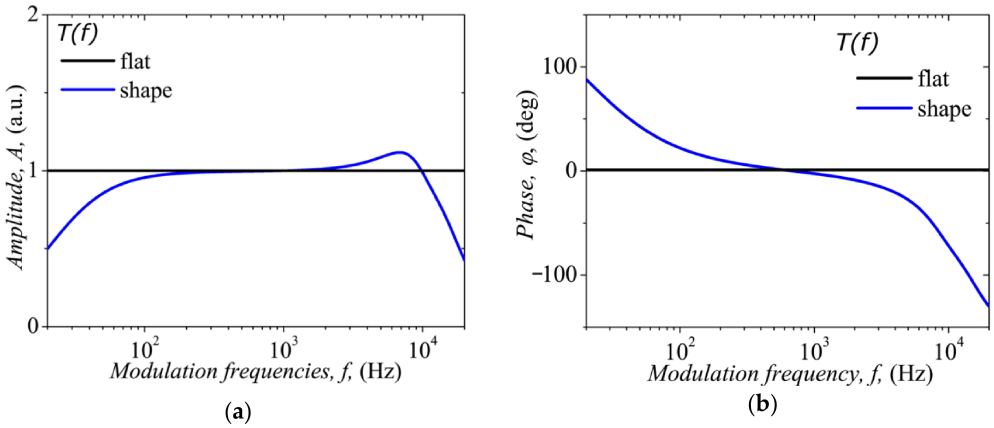



**Figure 1.** Representative elements of the operator family $T(f,\theta)$: (**a**) amplitude and (**b**) phase of the detector transfer function, together with the ideal flat response. The curves illustrate the low-parametric structure of the transfer function and its smooth frequency dependence [1]. Reproduced from M. I. Jordovic-Pavlovic et al., Computationally intelligent description of a photoacoustic detector, Optical and Quantum Electronics, vol. 52, art. 246, Springer Nature, 2020, with permission from Springer Nature Customer Service Centre GmbH. Not covered by the CC BY licence; reproduced with permission.

What is essential is that the detector influence is multiplicative in the frequency domain and parameterized by a low-dimensional vector $\theta$. In discrete form, the measurement yields complex-valued samples

$$S(f_k), \qquad k = 1, \dots, N, \tag{15}$$

which can be interpreted as elements of the Hilbert space $H = \mathbb{C}^N$. Within the operator-theoretic framework introduced above, the measurement process is therefore modeled as

$$\mathrm{y} = M(\theta)\,\mathrm{x},$$

where $x$ corresponds to the ideal signal and $M(\theta)$ represents the detector-induced transfer operator. In the frequency-domain representation, the transfer function $T(f,\theta)$ defines this operator as a multiplication operator, namely

$$(M(\theta)x)(f_k) = T(f_k,\theta)\,x(f_k), \qquad k = 1, \dots, N.$$

In particular, $M(\theta)$ is a bounded linear operator on $H = \mathbb{C}^N$.

This example satisfies the structural assumptions of the framework introduced in Section 2: the operator family is parameterized by a finite-dimensional vector, so that for a fixed reference signal its admissible variations generate a set of possible measured signals. The analysis of Section 2 can therefore be applied to identify the spectral regions in which the measured signal is most sensitive to the detector response.

### *3.2. Numerical Results*

#### 3.2.1. Dataset Description

In order to illustrate the proposed framework, a synthetic dataset was generated using the theoretical PA model described in Equations (10)–(14). The numerical simulations produce frequency-domain measurements corresponding to different parameter realizations of the transfer operator [35]. The inputs of the simulation include material parameters and

microphone characteristics. Aluminum samples coated with a thin absorbing layer were considered, with geometrical and thermal parameters summarized in Table 1.

**Table 1.** Theoretical values for the aluminum sample.

| Characteristic | Spread | Aluminum |
|---|---|---|
| Thermal conductivity $[\mathrm{Wm^{-1}K^{-1}}]$ | 70 | 210 |
| Thermal diffusivity $[\mathrm{m^2s^{-1}}]$ | $2.5 \times 10^{-5}$ | $8.6 \times 10^{-5}$ |
| Thermal relaxation time [s] | $10^{-4}$ | $10^{-12}$ |
| Absorption coefficient $[\mathrm{m^{-1}}]$ | $10^{8}$ | $145 \times 10^{6}$ |

Three commercially available microphones (ECM30B, ECM60, WM66) were modeled, resulting in three distinct operator families. In addition, an ideal microphone with an approximately flat frequency response was introduced as a reference operator, Figure 1. The ideal case corresponds to a transfer function that does not introduce frequency-dependent distortion and therefore serves as a baseline for comparison.

For each operator family, measurements were generated over the same discrete frequency grid, yielding complex-valued vectors in $H = \mathbb{C}^N$. The dataset thus consists of multiple realizations

$$\mathrm{y}^{(\mathrm{i})} = \mathrm{M}\left(\theta^{(\mathrm{i})}\right)\mathrm{x},$$

obtained by varying the operator parameters within their admissible ranges.

The admissible parameter ranges for the ECM30B ensemble are those of the database of [36]. These ranges were established by combining measurements of different samples obtained with the same microphone [36–38], measurements of the same sample obtained using three different microphones [39], and information from the available manufacturers' data sheets, which provide only amplitude-response characteristics. The parameters form a full grid: $f_2$ takes three values (23.75, 25, and 26.25 Hz, i.e., 25 Hz ± 5%); $f_3$ and $f_4$ take ten equidistant values each, in the ranges 8930–9866 Hz and 13,965–15,432 Hz, respectively; $\xi_3$ and $\xi_4$ take fifteen values each, irregularly distributed between 0.015 and 0.99. This gives $K = 3 \times 10 \times 10 \times 15 \times 15 = 67{,}500$ records, each consisting of 200 amplitude and 200 phase samples on the same frequency grid [10 Hz–100 kHz; for all three classes of microphone], i.e., 400 features.

#### 3.2.2. Eigen-Based Instrument-Sensitivity Subspace

As a direct numerical realization of the construction of Section 2, the covariance eigendecomposition of Equations (5) and (6) was carried out on the ECM30B ensemble ($K = 67{,}500$ realizations, standardized as described in Section 2.3, so that $\Sigma$ is the correlation matrix of the ensemble), without using the operator parameters $\theta$ at any stage. Table 2 reports the resulting eigenvalue spectrum and the cumulative variance fraction $\eta_k$.

The spectrum decays sharply: four modes already capture 95.5% of the total instrument-induced variability ($\eta_4 = 95.5\%$), and $k = 7$ captures $\eta_7 = 98.8\%$, essentially matching the smallest $k$ for which $\eta_k$ exceeds a 99% threshold ($k = 8$); this data-driven range, $k \approx 7$–8, is adopted below as the working dimension for the case study of Section 3.2.4. The dominant eigenvectors are not aligned with a single operator parameter: the leading two modes ($\eta_2 = 76\%$) are correlated predominantly with $f_2$ and $\xi_3$, while $f_3$, $f_4$ and $\xi_4$ become dominant only from the third mode onward. This is consistent with $f_2$ taking only three admissible values in the present ensemble, against ten or more for the remaining parameters, and illustrates a limitation already noted in Remark 1: the eigenvectors of $\Sigma$ reflect the relative amount of variance each parameter happens to induce over the sampled admissible ranges, not the number of instrumental parameters as such.

**Table 2.** Eigenvalue spectrum and cumulative variance fraction $\eta_k$ of the correlation matrix $\Sigma$ for the ECM30B ensemble.

| $k$ | $\lambda_k$ | $\eta_k$ [%] |
|---|---|---|
| 1 | 165.07 | 41.27 |
| 2 | 139.53 | 76.15 |
| 3 | 51.65 | 89.06 |
| 4 | 25.88 | 95.53 |
| 5 | 7.78 | 97.48 |
| 6 | 3.33 | 98.31 |
| 7 | 1.89 | 98.78 |
| 8 | 1.36 | 99.12 |
| 9 | 1.04 | 99.38 |
| 10 | 0.59 | 99.53 |

Thresholds of 95%, 98%, 99% and 99.5% on $\eta_k$ correspond to $k = 4$, 6, 8 and 10, respectively, so the criterion alone does not fix $k$. The threshold in Section 2.4 is an example of a criterion and not a fixed rule, and we use $k = 7$ ($\eta_7 = 98.8\%$), which is within 0.3 percentage points of the 99% threshold ($k = 8$). The choice is not critical: Section 3.2.5 shows that for $k = 6$–10, including $k = 8$, the same band (indices 148–160) is obtained.

Figure 2 shows the resulting frequency-resolved map $S_{\text{inst}}(\omega_n)$ for $k = 7$, computed separately for the amplitude and phase components. Over most of the spectrum $S_{\text{inst}}$ is close to 1, indicating that the seven dominant modes reconstruct the variability of essentially every frequency channel. Two narrow bands depart from this pattern: in amplitude, indices 148–160 (minimum $S_{\text{inst}} \approx 0.57$ at index 159), and in phase, the same index range (minimum $S_{\text{inst}} \approx 0.78$ at index 148). These are the frequencies whose instrument-induced variability is least redundant with the rest of the spectrum, and they are therefore expected to carry distinctive information about the operator parameters; this is checked directly against the correlation-based analysis of Sections 3.2.3 and 3.2.4.

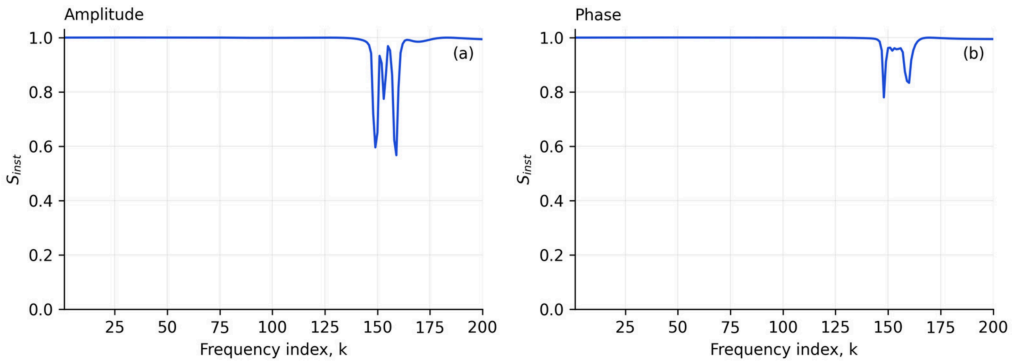



**Figure 2.** Frequency-resolved map $S_{\text{inst}}(\omega_n)$ for $k = 7$, for the amplitude (**a**) and phase (**b**) components of the ECM30B ensemble. Values close to 1 indicate that the dominant seven-mode subspace reconstructs the (standardized) variability of that frequency almost completely; the narrow dip near indices 148–160 marks the band that requires additional modes.

We stress that principal components are statistical constructs, not physical modes. A loading $v_j(\omega_n)$ indicates the contribution of the frequency $\omega_n$ to the $j$-th component; it does not mean that the frequency is the component, nor that the component corresponds to a single physical mechanism. Accordingly, sensitive frequency regions are identified in this paper only through the index $S_{\text{inst}}$ of Equation (9) and, in Section 3.2.3, through the correlation analysis, and eigenmodes are not identified with individual features.

3.2.3. Correlation-Based Selection of Spectral Features for Parameter Identification

The purpose of this section is to illustrate numerically how the information on the operator parameters is distributed over the measurement space $H = \mathbb{C}^{200}$, and to select, by a supervised correlation analysis, a small number of spectral features from which these parameters can be determined. Each simulated dataset consists of complex-valued measurements

$$S_k = A(f_k)\, e^{j\varphi(f_k)}, \qquad k = 1, \ldots, 400, \tag{16}$$

representing discrete samples of the frequency-domain response.

To analyze the structure of the measurement space, all amplitude and phase components are first normalized to ensure numerical comparability. The full correlation matrix of the 400-dimensional feature vector is then computed and examined. The resulting correlation structure reveals strongly correlated clusters of frequency components, indicating substantial redundancy and suggesting a strongly structured, low-dimensional variability, as further shown by the numerical results presented in the following section. This observation is consistent with the expectation that variations of a low-parametric operator family generate strongly structured variability in the measurement space. The correlation analysis used here is a supervised step that complements the covariance-based construction of Section 2: it uses the parameters θ to identify, from the simulated ensemble, the representative spectral coordinates from which they can be determined.

Complex and real-valued representations. The framework of Section 2 is formulated for complex vectors in $H = \mathbb{C}^N$ with $N = 200$, whereas the numerical analysis uses the 400-dimensional real vector $(|y(\omega_1)|, \ldots, |y(\omega_{200})|, \arg y(\omega_1), \ldots, \arg y(\omega_{200}))$. The map $y \mapsto (|y|, \arg y)$ is nonlinear and therefore not equivalent to a linear transformation of $H$. For a fixed reference signal $x$ it acts on the multiplication operator in a simple way: $|y_n| = |T(\omega_n;\theta)|\,|x_n|$ and $\arg y_n = \arg T(\omega_n;\theta) + \arg x_n$ (modulo $2\pi$; the phase in the database is unwrapped and expressed in degrees), so amplitude components are scaled and phase components shifted by quantities that depend on $\theta$ only through $T$. The statements of Sections 2.1 and 2.2 (structure of the operator family, multiplicative action, ensemble generated by admissible $\theta$) refer to $H$. Equations (5)–(9) are algebraic identities of principal component analysis and hold for any real feature vector; they were applied to the amplitude–phase vector, for which $\Sigma$ is real symmetric, and all numerical results of Sections 3.2.2–3.2.5 refer to this representation unless stated otherwise. The link with the complex operator is thus the componentwise relation above; we do not claim that the eigen-structure of the amplitude–phase representation coincides with that of the complex one. A check with the real and imaginary parts of $y$, which are linear functions of $y$, is given in Section 3.2.5.

Before the inverse analysis of the sample properties can begin, the contribution of the measurement chain has to be separated from the measured signal. According to Equation (14), the measured signal is the product of the pressure generated by the sample and the transfer function of the detector, $S(f) = \tilde{p}_{\mathrm{tot}}(f)T(f)$. If the transfer function $T(f)$ is known, that is, if the parameters $\theta = (f_2, f_3, f_4, \xi_3, \xi_4)$ of Equation (13) are known, the signal that originates from the sample alone is obtained from the measured one as $\tilde{p}_{\mathrm{tot}}(f) = \frac{S(f)}{T(f)}$ at the frequencies where $|T(f)|$ is not close to zero, and only this signal enters the inverse reconstruction. The determination of the transfer characteristic of the detector is therefore itself an identification (calibration) problem that precedes, or accompanies, the inversion of the sample properties, and the regression model of our earlier work [36], summarized below, addresses this problem: it estimates $\theta$ from the amplitude and phase of the measured response, and a small number of spectral samples can suffice for this purpose. The finding that the instrument-induced variability is effectively low-dimensional, with about seven dominant modes (Section 3.2.2), motivates the reduction of the input vector of the regression model: if the response varies within a subspace of such a small dimension, a small number

of spectral samples may suffice to determine $\theta$. The reduced set of seven features is then selected by the supervised procedure described in Section 3.2.4; the agreement of its size with the number of modes is a consistency of the two analyses and not a derivation of one from the other. The sensitivity map is a diagnostic step that precedes this procedure; it does not estimate $\theta$ and does not solve an inverse problem, but it indicates the frequency regions in which the instrument has to be taken into account and in which the uncertainty of $\theta$ affects the response most.

To quantify how much operator-specific information is retained in reduced representations, we introduce a regression mapping

$$\Phi : H \to \mathbb{R}^5, \tag{17}$$

which associates measured signals with the parameter vector $\theta = (f_2, f_3, f_4, \xi_3, \xi_4)$ characterizing the transfer operator.

The regression model, previously developed and validated in our earlier work [36], is used here as a quantitative probe and not as a new identification method: if a reduced feature subset determines the operator parameters with accuracy comparable to that obtained using the full 400-dimensional representation, then this subset captures the dominant operator-induced variability. The regression procedure is therefore used as an empirical check of the correlation-based selection of features rather than as a conceptual component of the framework.

For completeness, the model of [36] is summarized. It is a fully connected feed-forward network with 400 inputs (200 amplitudes and 200 phases), two hidden layers of 30 and 17 neurons with tanh activation, and five outputs $(f_2, f_3, f_4, \xi_3, \xi_4)$. Inputs and outputs are normalized by dividing each element by its maximum absolute value over the database; the weights are initialized by the Xavier scheme; the mean squared error is minimized with the Adam optimizer ($\beta_1 = 0.9$, $\beta_2 = 0.999$, $\varepsilon = 10^{-8}$), a learning rate of $10^{-4}$, a mini-batch of 32, and 3000 epochs. The 67,500 records (Section 3.2.1) were randomly shuffled and divided into 57,500 training, 5000 validation, and 5000 test records. The accuracy is the percentage of predicted parameter values whose deviation from the true value is below 5% (experimental request), and the average deviation of each parameter, as a percentage of its true value, is reported alongside it (Table 3). The value of 98.84% in Table 3 is the cross-validation accuracy on the 5000-record test set of [36]. The robustness of the network to random noise of ±5% in the input was examined in [36]. For the reduced inputs, the same procedure is used with the input layer reduced to the selected features [hidden layers and hyperparameters unchanged].

**Table 3.** The performance of the reference model, Equation (17).

| **Accuracy [%]** | **Average Deviation from the Accurate Value, Expressed as a Percentage of the Accurate Value** | | | | | **Prediction Time [ms]** |
|---|---|---|---|---|---|---|
| | $f_2$ | $f_3$ | $f_4$ | $\xi_3$ | $\xi_4$ | |
| 98.84 | 0.036 | 0.064 | 0.039 | 0.668 | 0.744 | 14 |

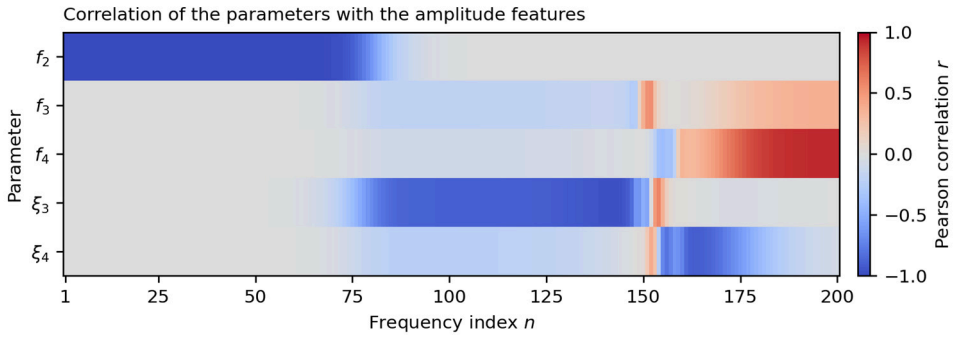
To assess robustness, the analysis is performed on three microphone classes (ECM30B, ECM60, and WM66). This cross-class comparison examines whether the identified low-dimensional structure reflects intrinsic operator geometry rather than dataset-specific artifacts.

Through this analysis, we illustrate that the correlation structure of the measurement space is strongly organized: the information on the operator parameters is concentrated in a small subset of frequency-domain regions.

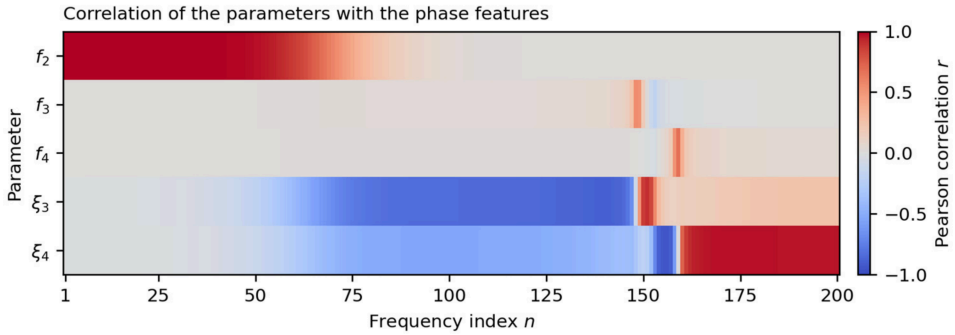
3.2.4. Results

To assess the internal structure of the PA measurement space and identify a minimal set of frequency-domain features that sufficiently characterize the microphone operator $M$, we first evaluate the regression-based parameter recovery using the full 400-dimensional input. ECM30B was selected as a representative reference case; however, the analysis is not specific to this microphone, and any of the considered microphone models could have been used instead. Table 3 reports the estimation accuracy and average relative deviation (in percent) for each of the five operator parameters. These values provide a baseline for all reduced representations.

To examine how information about the operator parameters is distributed across the spectrum, Figure 3 displays the Pearson correlation between each target parameter $f_2$, $f_3$, $f_4$, $\xi_3$, $\xi_4$ and the 200 amplitude features (Figure 3a) and 200 phase features (Figure 3b). Each row corresponds to one output parameter, while the horizontal axis indexes the frequency-domain input features. The color scale indicates the sign and magnitude of the correlation. Figure 3 reveals several structural properties. Both amplitudes and phases exhibit narrow frequency intervals where the correlation magnitude is high. These regions identify frequencies at which the measurement operator is most sensitive to changes in a given parameter. Amplitude features typically form smooth positive or negative bands, whereas phase features show sharper transitions, reflecting complementary sensitivity to the operator behavior. The extent of this sensitivity varies by parameter: for $f_3$ and $f_4$, pronounced correlation is confined to a small subset of frequencies, while for $f_2$, $\xi_3$ and $\xi_4$, a substantially larger fraction of the spectrum shows non-negligible correlation. Moreover, each output parameter produces a distinct correlation pattern, suggesting that different spectral regions encode different aspects of the transfer behavior.




(**a**)




(**b**)

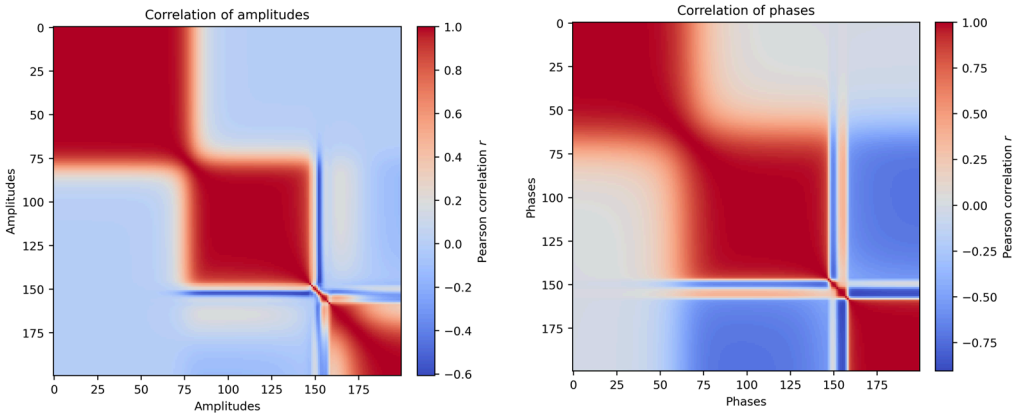
**Figure 3.** The correlation between the five operator parameters (output space) and the 200 amplitude features (**a**) and 200 phase features (**b**).

Based on Figure 3, the spectral regions that carry significant linear dependence on each operator parameter were identified. Table 4 summarizes these informative amplitude and phase ranges (indices refer to the discrete frequency grid).

**Table 4.** Informative amplitude and phase intervals for operator parameters.

| Target Parameter | Amplitude | Phase |
|---|---|---|
| $f_2$ | 0–70 | 0–60 |
| $f_3$ | 151 | / |
| $f_4$ | 181–199 | 158 |
| $\xi_3$ | 85–143 | 74–142, 150 |
| $\xi_4$ | 162–164 | 154–156, 161–200 |

Figure 4 shows the internal correlation structure among the 200 amplitude features (left panel) and the 200 phase features (right panel). Each heat map displays the pairwise Pearson correlation between features indexed by frequency, revealing the geometry of the measurement space prior to any reduction. Several patterns are clearly visible. Both amplitude and phase matrices exhibit large contiguous blocks of strong positive correlation. These blocks correspond to frequency intervals within which features are strongly correlated and therefore convey nearly identical information about the operator for the purpose of linear estimation. The smooth structure of the blocks indicates that the microphone operator effect is almost constant in these ranges. The blocks are separated by transition lines where correlations change rapidly. Such boundary frequencies indicate shifts in operator sensitivity and are therefore informative. Both matrices also show regions of strong negative correlation between separated spectral intervals, indicating opposing dependencies across frequency bands. In such cases, retaining both strongly negatively correlated features is unnecessary from the standpoint of linear dependence. Overall, the combination of large coherent blocks and sparse transition regions suggests that the amplitude and phase feature spaces contain only a small number of effective degrees of freedom, which motivates a strategy based on (i) selecting representative features from each correlation block and (ii) including additional features near transition boundaries.




(**a**) (**b**)

**Figure 4.** Correlation structure among the 200 amplitude features (**a**) and the 200 phase features (**b**).

Figure 5 presents the cross-correlation matrix between the 200 amplitude features (horizontal axis) and the 200 phase features (vertical axis), revealing how operator-related sensitivity is distributed jointly across amplitudes and phases.

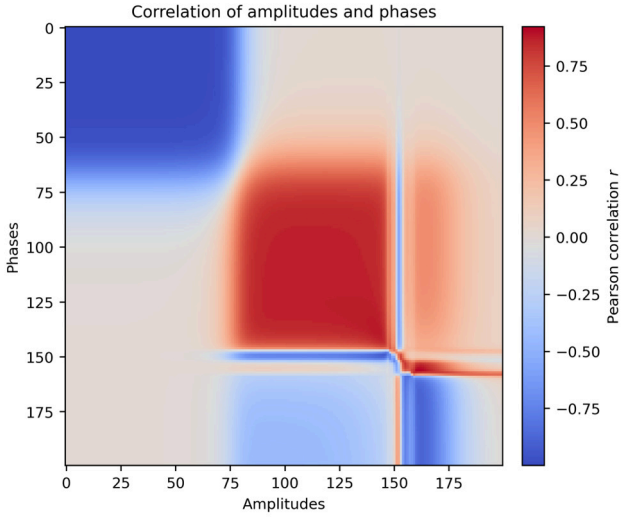



**Figure 5.** Cross-correlation matrix between the 200 amplitude features (horizontal axis) and the 200 phase features (vertical axis).

A large central region of strong positive correlation indicates frequency ranges where amplitude and phase vary in a coordinated manner under changes of $M$. Conversely, regions of strong negative correlation indicate frequency bands where amplitude and phase respond with opposite signs. Narrow vertical and horizontal transition lines mark frequencies at which the amplitude–phase relationship changes abruptly, again highlighting spectral transition points where the operator behavior changes character. The combined block structure confirms substantial redundancy across amplitude–phase pairs and supports selecting a mixed set of amplitude and phase features rather than treating the two domains independently.

Selection procedure. The seven features were selected as follows; the regression is used only to check the result. (i) *Blocks:* in Figure 4, the features form blocks of mutually high correlation (light rectangles; $|r| \geq 0.85$); within a block the features are interchangeable for linear estimation, so one representative is kept, taken at the centre of the block. (ii) *Coverage:* the representatives are chosen so that each operator parameter is represented in an informative interval of Table 4: $\varphi(33)$ for $f_2$, $\mathrm{A}(151)$ for $f_3$, $\mathrm{A}(186)$ for $f_4$, $\varphi(105)$ and $\varphi(150)$ for $\xi_3$, and $\varphi(154)$ and $\varphi(186)$ for $\xi_4$. Informative intervals consisting of a single index are retained as they are, whereas wider intervals are represented by the centre of the block. Two of the selected features, $\mathrm{A}(151)$ and $\varphi(150)$, are of the first kind and lie at transitions between correlation blocks (Figure 4): $\mathrm{A}(151)$ is the only amplitude feature in an informative interval for $f_3$, and $\varphi(150)$ is an isolated informative phase index for $\xi_3$. At such transitions the correlation structure changes rapidly, so neighbouring features are not interchangeable as they are within a block; omitting $\mathrm{A}(151)$ or $\varphi(150)$ lowers the accuracy by about 5 and 2 percentage points, respectively. Both lie in the band where the eigen-analysis gives the lowest $S_{\mathrm{inst}}$ (0.93 and 0.96 for $k = 7$, Section 3.2.2). (iii) *Check:* the regression probe then shows how close the resulting set comes to the accuracy of the full input. This last step is empirical: the final set is not claimed to be unique or optimal. The correlation tools used here are conventional; their role in this paper is not that of a new selection criterion but that of a supervised analysis that is complementary to the unsupervised map of Section 3.2.2 (see the discussion below). The steps are summarized in Algorithm 1.

Based on the combined analysis of Figures 3–5, a seven-dimensional mixed feature set (five phases and two amplitudes) was identified to represent the dominant operator-related variability; the dimension $k = 7$ was not derived from, but turned out to be close to, the data-driven threshold $\eta_k$ obtained independently from the eigen-based analysis of

Section 3.2.2 ($k \approx 7$–8). The selected features are: $A(151)$, $A(186)$, $\varphi(33)$, $\varphi(105)$, $\varphi(150)$, $\varphi(154)$, $\varphi(186)$. Here, $A$ and $\varphi$ denote the amplitude and phase components, respectively, while the numbers in parentheses indicate the indices of the corresponding frequency points in the 200-point frequency grid spanning 10 Hz to 100 kHz, each point carrying an amplitude and a phase (400 features). The number of selected features was fixed by the trade-off between dimension and accuracy reported in in Section 3.2.5, and not by $k$; it is not claimed to reflect the number of operator parameters or to be a universal property of the operator, and the remaining features are not thereby implied to be irrelevant for the physical signal.

**Algorithm 1.** Selection of the reduced feature set (supervised procedure of Sections 3.2.3 and 3.2.4).

**Input:** ensemble of responses ($N \times 400$ matrix of amplitude and phase features), the parameters $\theta = (f_2, f_3, f_4, \xi_3, \xi_4)$, and the block threshold $|r| \geq 0.85$.
1. Standardize the features and compute (a) the correlation matrix among the features (Figures 4 and 5) and (b) the correlation of every feature with each parameter $\theta_j$ (Figure 3).
2. Informative intervals. For each $\theta_j$, record the amplitude and phase indices at which the correlation with $\theta_j$ is significant (Table 4).
3. Blocks. Group neighbouring features with mutually high correlation ($|r| \geq 0.85$) into blocks (Figure 4); within a block the features are interchangeable for linear estimation.
4. Representatives. For every $\theta_j$, take the centre of the block that lies in its informative interval; if an informative interval consists of a single index, or an isolated index at a block transition, keep that index. Merge the choices over all parameters, so that each $\theta_j$ is covered by at least one feature (here 7 features).
5. Check. Train the regression probe $\Phi$ on the selected features and compare its accuracy with that for the full input; if it is unsatisfactory, return to step 4 with another representative of the uncovered block.
6. Diagnostic (optional). Compare the selected indices with the unsupervised map $S_{\text{inst}}$ (Section 3.2.2, Figure 6); this comparison does not change the selection.
Output: the reduced feature set A(151), A(186), $\varphi(33)$, $\varphi(105)$, $\varphi(150)$, $\varphi(154)$, $\varphi(186)$. The set is not claimed to be unique or optimal.

Using only these seven features, the regression-based parameter recovery achieves an accuracy of 97.27%, compared to 98.84% using the full 400-dimensional input. Thus, seven of the 400 features (1.75%) suffice to retain most of the accuracy for the purpose of estimating $f_2, f_3, f_4, \xi_3, \xi_4$. We stress that this is a statement about the accuracy of the regression probe, not about the linear dependence of the full feature space or about the information content of the discarded features. The preservation of accuracy under such strong reduction is consistent with the premise of the framework, namely that the sensitivity to the parameters of the transfer operator is concentrated in a small number of spectral regions (the informative intervals of Table 4). It is consistent with this premise, but it is not a proof of it.

To examine stability across operator classes, the same procedure was applied to two additional microphone classes used in PA experiments: ECM60 and WM66. In both cases, the correlation patterns exhibited the same qualitative structures observed for ECM30B: coherent correlation blocks, sharp transition boundaries, and clear amplitude–phase complementarity. The corresponding correlation maps are omitted for brevity due to space limitations. The regression accuracies obtained with the reduced seven-feature sets are given in Table 5.

Applying the same selection principles yields a seven-dimensional feature subset for each microphone class. Although the specific frequency indices vary slightly across devices,

the selected features consistently originate from the same operator-sensitive spectral regions. The resulting parameter recovery accuracies remain above 97% for all three microphones.

**Table 5.** The performance of the regression model on the reduced input data set.

| Microphone Class | Accuracy [%] | Average Deviation from the Accurate Value, Expressed as a Percentage of the Accurate Value | | | | | Prediction Time [ms] |
|---|---|---|---|---|---|---|---|
| | | $f_2$ | $f_3$ | $f_4$ | $\xi_3$ | $\xi_4$ | |
| ECM30B | 97.27 | 0.088 | 0.178 | 0.100 | 1.611 | 1.723 | 14 |
| ECM60 | 97.53 | 0.076 | 0.192 | 0.104 | 1.266 | 1.679 | 14 |
| WM66 | 97.56 | 0.109 | 0.183 | 0.101 | 1.411 | 1.488 | 14 |

From the standpoint of the framework of Section 2, these results provide empirical support for the existence of an effectively low-dimensional instrument-sensitive structure in the measurement space and locate the spectral regions of pronounced instrumental sensitivity (Table 4 and the selected features above).

The map of Section 3.2.2 and the correlation-based feature selection of this section answer two different questions about the same instrument and the same ensemble, and they are complementary. The map is diagnostic and unsupervised: it is computed from the ensemble of responses, which depends on the admissible set of parameters but not on the values of θ attached to the individual responses, and it localizes the frequencies at which the uncertainty of the instrumental response cannot be neglected. The correlation analysis uses θ: it identifies the spectral samples from which the instrument parameters, and hence the transfer function, can be determined, and it is used here to select a small number of features; it is not an alternative method for locating sensitivity. In the case study the map (Figure 2) shows its most pronounced departure from redundancy in indices 148–160, with a minimum near index 159. This is the band that Table 4 identifies as informative for $f_3$ (amplitude index 151) and, adjacently, for $\xi_3$ and $\xi_4$, and the data-driven threshold $\eta_k$ of Section 3.2.2 gives a working dimension ($k \approx 7$–$8$) close to the value used in this case study. The agreement holds at the level of the sensitive band and of the parameter-wise informative regions of Table 4; it does not extend to the final seven-feature set. A frequency with a low $S_{\text{inst}}$ is one whose variation cannot be represented by the dominant modes, which is characteristic of local resonant behaviour, whereas a frequency with $S_{\text{inst}}$ close to 1 is determined by the dominant modes and is therefore a good indicator of the parameters that the modes encode jointly. This explains why three of the selected features lie in the band found by the map (A(151), $\varphi$(150), $\varphi$(154)) and four outside it (A(186), $\varphi$(33), $\varphi$(105), $\varphi$(186)), with $S_{\text{inst}} \approx 1$. A partial overlap is to be expected: the seven features by which the transfer function is determined must capture how the instrument responds to its parameters, and this response is strongest where the map finds the instrument most sensitive. Accordingly, each of $f_3$, $\xi_3$ and $\xi_4$ has a selected feature in the band, whereas the influence of $f_2$ and $f_4$, and the wider informative ranges of $\xi_3$ and $\xi_4$ (Table 4), extend to frequencies outside it. This is also why the supervised correlation analysis is used alongside the map: the map shows where the instrumental influence cannot be neglected, and the correlation analysis shows which spectral samples determine the instrument parameters; the two parts of the paper address these two sides of the same problem. As a further check, the regression probe was also trained on the seven features with the lowest $S_{\text{inst}}$, that is, on the features chosen from the map alone (A(148), A(149), A(150), A(153), A(158), A(159), $\varphi$(148)). Its accuracy is 87.85%, against 97.27% for the selected set: these features are concentrated in the band and do not cover all of the parameters (Table 4).

Figure 6 summarizes this relation. On the logarithmic frequency grid, $f_n = 10 \cdot 10^{4(n-1)/199}$ Hz, the sensitive band 148–160 identified without any use of θ corre-

sponds to approximately 9.0–15.7 kHz, i.e., to the range that contains the acoustic resonances $f_3$ and $f_4$ of the microphone, where the operator $M(\omega;\theta)$ changes its behaviour most strongly. The features that the supervised analysis cannot do without, $\mathrm{A}(151)$ and $\varphi(150)$, lie in this band, together with $\varphi(154)$, whereas the remaining four features lie outside it; they are determined by the coverage of the informative intervals of Table 4, not by the eigen-sensitivity.

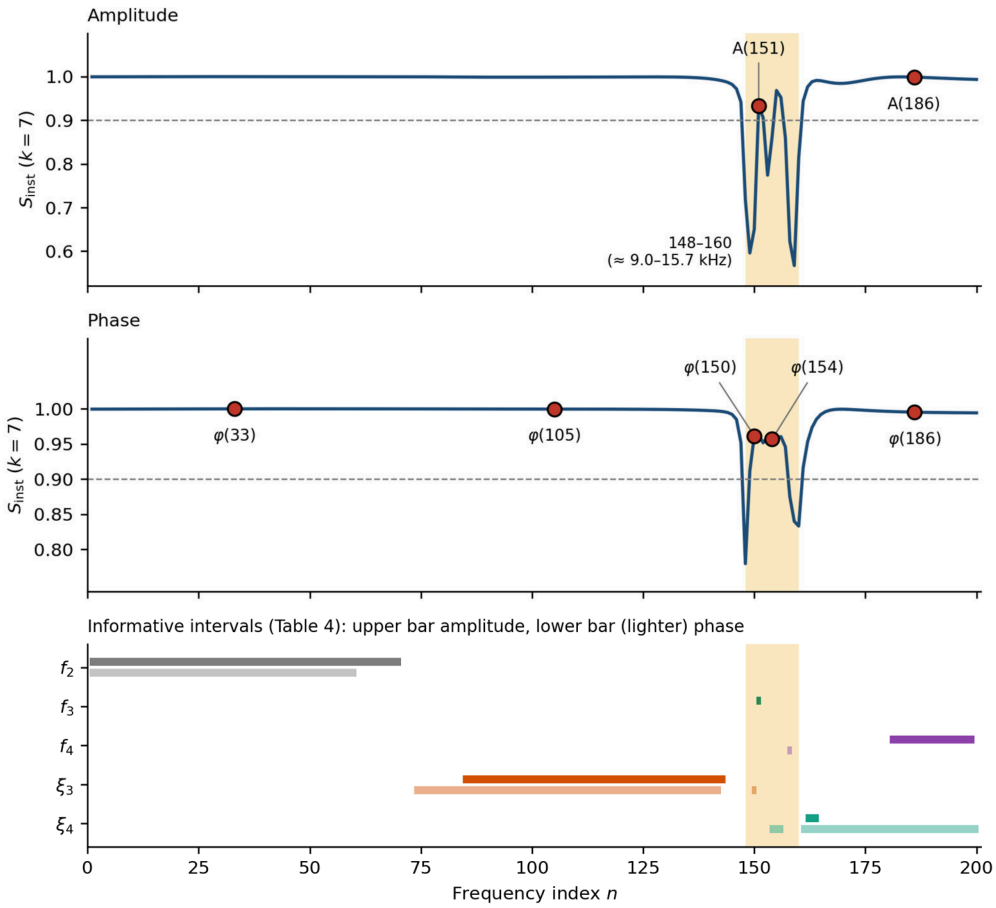



**Figure 6.** Frequency-resolved instrument-sensitivity map $S_{\mathrm{inst}}$ for $k = 7$ (amplitude and phase), the informative intervals of Table 4 and the seven selected features. The shaded band, indices 148–160, corresponds to approximately 9.0–15.7 kHz on the logarithmic frequency grid and contains the resonances $f_3$ and $f_4$; the dashed line marks the flagging threshold 0.9. Dots: $\mathrm{A}(151)$, $\mathrm{A}(186)$, $\varphi(33)$, $\varphi(105)$, $\varphi(150)$, $\varphi(154)$, $\varphi(186)$. **Lower panel**: upper bar of each pair, amplitude; lower (lighter) bar, phase.

### 3.2.5. Robustness of the Sensitivity Map and of the Feature Count

This section examines how robust the main numerical statements are to the modelling choices discussed above: the dimension $k$ and the flagging threshold $\tau$, the standardization, and the number of selected features. Table 6 reports how the map of Figure 2 changes with $k$ ($\eta_k$ from 95.5% to 99.5%) at the flagging threshold $S_{\mathrm{inst}} < 0.9$. Increasing $k$ raises $S_{\mathrm{inst}}$ monotonically, so fewer frequencies fall below the threshold, but their location does not change: for $k = 6$–$10$ every flagged frequency, in amplitude and in phase, lies in the band 148–160, and the minima stay within indices 148–159. Only for $k = 4$ and 5, which capture less than 97.5% of the variance, does the flagged set widen, to indices 142–161. The rank correlation (Spearman) of the maps with that for $k = 7$ is 0.93–0.98 for $k = 5$–$10$ ($k \neq 7$). The dependence on $\tau$ is similar: for $k = 7$ the flagged sets are indices 148–159 in amplitude (6 frequencies) and 148 in phase (1 frequency) for $\tau = 0.8$; 148–160 (9) and

148–160 (4) for $\tau = 0.9$; and 147–161 (13) and 148–161 (7) for $\tau = 0.95$. The choice between $k = 7$ and $k = 8$ (the first value above the 99% threshold) therefore does not affect the identified band; Figure 7 shows the eigenvalue spectrum.

**Table 6.** Dependence of the sensitivity map on $k$ for the ECM30B ensemble (flagging threshold $S_{\text{inst}} < 0.9$; $n$ is the number of flagged frequencies; indices refer to the 200-point frequency grid).

| k | $\eta_k$ [%] | Amplitude: min $S_{\text{inst}}$ (Index) | Amplitude: n ($S_{\text{inst}} < 0.9$), Indices | Phase: min $S_{\text{inst}}$ (Index) | Phase: n ($S_{\text{inst}} < 0.9$), Indices | Spearman $\rho$ vs. k = 7 |
|---|---|---|---|---|---|---|
| 4 | 95.53 | 0.14 (152) | 16, 146–161 | 0.18 (148) | 18, 142–160 | 0.83 |
| 5 | 97.48 | 0.42 (148) | 16, 146–161 | 0.55 (149) | 9, 148–160 | 0.96 |
| 6 | 98.31 | 0.51 (158) | 13, 148–160 | 0.64 (159) | 5, 148–160 | 0.98 |
| 7 | 98.78 | 0.57 (159) | 9, 148–160 | 0.78 (148) | 4, 148–160 | 1.00 |
| 8 | 99.12 | 0.61 (149) | 6, 148–160 | 0.81 (148) | 3, 148–159 | 0.98 |
| 9 | 99.38 | 0.71 (150) | 5, 148–159 | 0.87 (148) | 1, 148 | 0.94 |
| 10 | 99.53 | 0.78 (148) | 4, 148–159 | 0.92 (159) | 0, – | 0.93 |

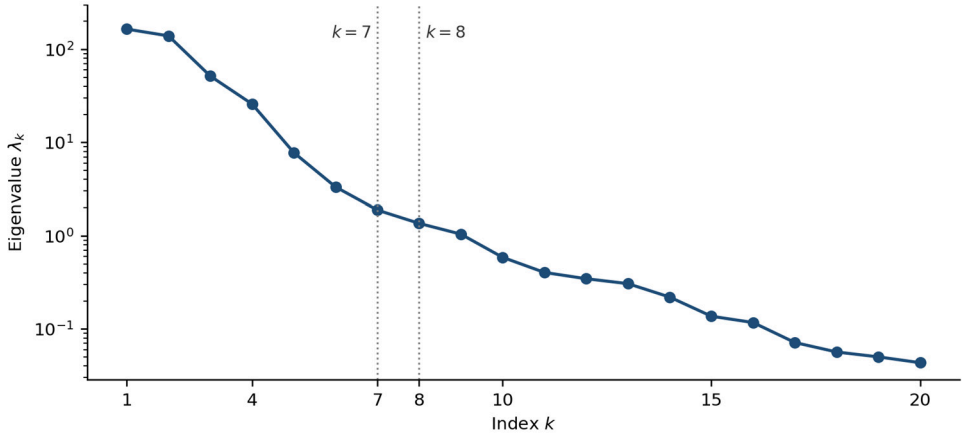



**Figure 7.** Eigenvalues $\lambda_k$ of the correlation matrix for the ECM30B ensemble ($k$ = 1–20, logarithmic scale); the dotted lines mark $k = 7$ and $k = 8$.

**Covariance versus correlation.** The first seven eigenmodes of the unstandardized covariance matrix capture 98.0% of the total variance ($k = 8$: 98.5%). The five largest diagonal elements of $\Sigma_7$ lie at amplitude indices 149, 148, 150, 158 and 159 and at phase indices 151, 152, 150, 155 and 156, that is, again in the band 148–160, but this ranking is not stable with $k$: for $k = 8$ the five largest amplitude elements move to indices 1–5. Normalized by the variance of each component, $[\Sigma_k]_{nn}/\Sigma_{nn}$ falls below 0.9 for 244 of the 400 components for $k = 7$ (165 amplitude and 79 phase components) and for 84 components for $k = 8$, against 13 and 9 flagged components, respectively, in the standardized map. Without standardization, the measure is therefore governed by the scale of individual components and loses its ability to single out a particular band, which justifies the use of the correlation matrix.

Real and imaginary parts. To check the dependence on the representation, the analysis was repeated for the real and imaginary parts of $y$ (computed from the amplitude and the phase, the latter given in degrees), which are linear functions of $y$. For $k = 7$ ($\eta_7 = 97.5\%$ in this representation) the flagged frequencies ($S_{\text{inst}} < 0.9$) are indices 148–160 for the imaginary part (10 frequencies; minimum 0.27 at index 159) and 147–161 for the real part (12 frequencies; minimum 0.37 at index 158), plus one isolated frequency (index 17), at which the standard deviation of the real part has a local minimum (0.034, against 0.11 and 0.13 at the neighbouring indices 16 and 18). The sensitive band is thus the same as in the amplitude–phase representation, although the maps differ in detail

(Spearman correlation 0.73 and 0.72 of the real and imaginary maps with the amplitude and phase maps, respectively).

Number of selected features. Table 7 reports the accuracy of the regression probe as a function of the number of input features. The largest gain in accuracy is obtained up to seven features (93.4% for five, 95.8–96.6% for six and 97.27% for seven), and the improvement then slows down (97.7% for eight and 97.8% for ten), compared with 98.84% for the full 400-feature input. The gain beyond seven features (0.4–0.5 percentage points) is small compared with the gain from five to seven (3.9 points), while the full input remains 1.6 points more accurate than the seven-feature set. The choice of seven features is thus a compromise between dimension and accuracy: it was fixed by this trade-off and not by $k$, and its proximity to $k \approx 7$–8 (Section 3.2.2) is noted but not used as a selection criterion. [All values except the seven-feature one are single evaluations on the test set; the seven-feature value is cross-validation mean ± SD, 97.27% ± 0.0025].

**Table 7.** Accuracy of the regression probe versus the number of input features (ECM30B).

| Number of Features | Accuracy [%] | Note |
|---|---|---|
| 5 | 93.4 | |
| 6 | 95.8–96.6 | Range over four evaluated six-feature sets |
| 7 | 97.27 | Selected set: A(151), A(186), $\varphi$(33), $\varphi$(105), $\varphi$(150), $\varphi$(154), $\varphi$(186) |
| 8 | 97.7 | |
| 10 | 97.8 | |
| 400 | 98.84 | Full input (Table 3) |

## 4. Conclusions

In this work, a mathematical framework has been developed for identifying frequency-dependent sensitivity of measured signals to unknown measurement-system response. The framework considers a family of measurement operators with a prescribed structural form but uncertain parameter values and quantifies the variability induced by admissible changes in the measurement operator.

The resulting covariance decomposition identifies the dominant directions in measurement space along which the measured signal is most sensitive to instrumental variations. These directions define a dominant instrument-sensitivity subspace, while the associated eigenvalue spectrum provides a quantitative measure of how the instrumental variability is distributed among the identified modes. Importantly, the dimensionality of this subspace is determined from the resulting variability structure rather than being imposed by the number of frequency samples.

The proposed framework is not intended to reduce the physical signal or to prescribe in advance which frequency intervals should be discarded. Instead, projection of the dominant instrument-sensitive modes onto the frequency domain provides a frequency-resolved representation of instrumental sensitivity. This representation identifies the spectral regions in which the measured signal is most affected by admissible uncertainty in the measurement response. Such information can subsequently be used to determine how different frequency regions should be treated in a particular inverse analysis, for example through exclusion, frequency-dependent weighting, or explicit uncertainty assignment.

In the photoacoustic case study, a regression probe recovers the five microphone parameters with 97.27% accuracy from seven features selected with the aid of the correlation analysis (97.53% and 97.56% for ECM60 and WM66), compared with 98.84% for the full 400-dimensional input of ECM30B. This result is supporting evidence that the identified spectral regions retain operator-relevant information. It is not a claim that the remaining

features are uninformative, the regression is not part of the proposed framework, and the seven-feature set is not claimed to be unique or optimal.

Although motivated by photoacoustic measurements, the formulation is not restricted to photoacoustics. It is applicable, in principle, to experimental problems in which the measurement system can be represented by a structurally constrained but incompletely known linear operator; however, the case study covers a single operator structure, and examples with other operator structures are left for future work. The photoacoustic case study demonstrates how a high-dimensional measured spectrum can exhibit a structured distribution of instrumental sensitivity and how this structure can be resolved without imposing a priori frequency truncation.

More generally, the results emphasize that discrepancies between theoretical predictions and experimental measurements may originate not only from the physical model but also from the measurement chain. Separating these two sources of variation is therefore an important prerequisite for interpreting measured data in inverse problems. The proposed framework provides a systematic way of mapping uncertainty in the measurement operator onto the measured-data space and, ultimately, onto the frequency domain, thereby supplying quantitative information that can be incorporated into subsequent inverse analysis.

The presented method provides a diagnostic basis for identifying frequency regions of dominant instrumental influence in simulated measurements of an instrument with an uncertain transfer function. It does not solve an inverse problem and does not claim to improve a specific inversion algorithm; the integration of the sensitivity map into inverse analysis, and its validation on measured data, remain future work. The parametrization of the case study is based on a comparison of the available manufacturer specifications and measurements, but the map itself has not been validated independently as a means of improving inverse analysis on new experimental data. The results of the regression probe support the analysis of the information structure of the specific model; they do not replace a test with an inverse algorithm.

**Supplementary Materials:** The following supporting information can be downloaded at: https://www.mdpi.com/article/10.3390/math14224241/s1, Figure S1: Number of flagged features and width of the flagged band as functions of the threshold $\tau$ and the number of modes k; Figure S2: Critical number of modes k* as a function of the frequency index; Table S1: Flagged indices for Sinst $< 0.9$ and for Rn $> \varepsilon$; Table S2: Flagged indices for the original database and for the database with Gaussian noise; Table S3: Accuracy of the individual networks, their mean $\pm$ standard deviation, and the ensemble in the independent tests; Table S4: Relative error of the ensemble for each output.

**Author Contributions:** M.J.P.: Data curation, Investigation, Methodology, Software, Visualization, Writing–original draft. S.G.: Conceptualization, Formal analysis, Investigation, Methodology, Supervision, Validation, Writing original draft, Writing–review & editing. M.N.P.: Conceptualization, Investigation, Methodology, Supervision, Validation, Writing original draft, Writing–review & editing D.C.: Conceptualization, Methodology, Supervision, Validation, Writing original draft, Writing–review & editing; E.S.: Formal analysis, Methodology, Supervision, Validation, Writing original draft, Writing–review & editing. D.M.: Conceptualization, Formal analysis, Methodology, Supervision, Validation, Writing original draft, Writing–review & editing; K.D.: Investigation, Methodology, Software, Visualization, Writing–original draft. All authors have read and agreed to the published version of the manuscript.

**Funding:** The authors acknowledge funding from the Ministry of Science, Technological Development and Innovation of the Republic of Serbia, through a grant to the Institute of Physics Belgrade, through Contract number 451-03-34/2026-03/200108 with the Faculty of Mechanical and Civil Engineering in Kraljevo, University of Kragujevac and Contract No. 451-03-33/2026-03/200017 with Vinca Institute of Nuclear Sciences, University of Belgrade.

**Data Availability Statement:** The data presented in this study are available on request from the corresponding authors.

**Conflicts of Interest:** The authors declare no conflicts of interest.

## References


1. Jordovic-Pavlovic, M.I.; Kupusinac, A.D.; Djordjevic, K.L.; Galovic, S.P.; Markushev, D.D.; Nesic, M.V.; Popovic, M.N. Computationally intelligent description of a photoacoustic detector. *Opt. Quantum Electron.* **2020**, *52*, 246. [CrossRef]
2. Ljung, L. *System Identification: Theory for the User*, 2nd ed.; Prentice Hall PTR: Upper Saddle River, NJ, USA, 1999.
3. Pintelon, R.; Schoukens, J. *System Identification: A Frequency Domain Approach*, 2nd ed.; IEEE Press/Wiley: Hoboken, NJ, USA, 2012. [CrossRef]
4. Yu, M.; Wang, W.; Wang, Y. Closed-Loop Continuous-Time Subspace Identification with Prior Information. *Mathematics* **2023**, *11*, 4924. [CrossRef]
5. Tarantola, A. *Inverse Problem Theory and Methods for Model Parameter Estimation*; Siam, Society for Industrial and Applied Mathematics: Philadelphia, PA, USA, 2004; ISBN 0-89871-572-5.
6. Kabanikhin, S.I. Definitions and examples of inverse and ill-posed problems. *J. Inverse Ill-Posed Probl.* **2008**, *16*, 317–357. [CrossRef]
7. Kaipio, J.; Somersalo, E. *Statistical and Computational Inverse Problems*; Springer: New York, NY, USA, 2005.
8. Engl, H.W.; Hanke, M.; Neubauer, A. *Regularization of Inverse Problems*; Springer: Dordrecht, The Netherlands, 2000.
9. Bungert, L.; Burger, M.; Korolev, Y.; Schönlieb, C.-B. Variational regularisation for inverse problems with imperfect forward operators and general noise models. *Inverse Probl.* **2020**, *36*, 125014. [CrossRef] [PubMed]
10. Hohage, T.; Werner, F. Error estimates for variational regularization of inverse problems with general noise models for data and operator. *Electron. Trans. Numer. Anal.* **2022**, *57*, 127–152. [CrossRef]
11. Hansen, P.C.; Sekii, T.; Shibahashi, H. The modified truncated SVD method for regularization in general form. *SIAM J. Sci. Stat. Comput.* **1992**, *13*, 1142–1150. [CrossRef]
12. Cui, T.; Martin, J.; Marzouk, Y.M.; Solonen, A.; Spantini, A. Likelihood-informed dimension reduction for nonlinear inverse problems. *Inverse Probl.* **2014**, *30*, 114015. [CrossRef]
13. Cui, T.; Marzouk, Y.M.; Willcox, K.E. Scalable posterior approximations for large-scale Bayesian inverse problems via likelihood-informed parameter and state reduction. *J. Comput. Phys.* **2016**, *315*, 363–387. [CrossRef]
14. Spantini, A.; Solonen, A.; Cui, T.; Martin, J.; Tenorio, L.; Marzouk, Y.M. Optimal low-rank approximations of Bayesian linear inverse problems. *SIAM J. Sci. Comput.* **2015**, *37*, A2451–A2487. [CrossRef]
15. Perrin, T.V.E.; Roustant, O.; Rohmer, J.; Alata, O.; Naulin, J.P.; Idier, D.; Pedreros, R.; Moncoulon, D.; Tinard, P. Functional principal component analysis for global sensitivity analysis of model with spatial output. *Reliab. Eng. Syst. Saf.* **2021**, *211*, 107522. [CrossRef]
16. Bergmann, T.G.; Welzel, M.O.; Jacob, C.R. Towards theoretical spectroscopy with error bars: Systematic quantification of the structural sensitivity of calculated spectra. *Chem. Sci.* **2020**, *11*, 1862–1877. [CrossRef] [PubMed]
17. Tarvainen, T.; Cox, B. Quantitative photoacoustic tomography: Modeling and inverse problems. *J. Biomed. Opt.* **2024**, *29*, S11509. [CrossRef] [PubMed]
18. Haltmeier, M.; Neumann, L.; Rabanser, S. Single-stage reconstruction algorithm for quantitative photoacoustic tomography. *Inverse Probl.* **2015**, *31*, 065005. [CrossRef]
19. Hirsch, L.; González, M.G.; Rey Vega, L. On the robustness of model-based algorithms for photoacoustic tomography: Comparison between time and frequency domains. *Rev. Sci. Instrum.* **2021**, *92*, 114901. [CrossRef] [PubMed]
20. Jolliffe, I. Principal Component Analysis. In *Encyclopedia of Statistics in Behavioral Science*; Everitt, B.S., Howell, D.C., Eds.; Wiley: Chichester, UK, 2005. [CrossRef]
21. Li, J.; Deng, Z.; Tang, Y.; Wang, S.; Yang, Z.; Luo, H.; Feng, W.; Zhang, B. Improved Bayesian Model Updating Method for Frequency Response Function with Metrics Utilizing NHBFT-PCA. *Mathematics* **2024**, *12*, 2076. [CrossRef]
22. Cvetković, N.; Lie, H.C.; Bansal, H.; Veroy, K. Choosing Observation Operators to Mitigate Model Error in Bayesian Inverse Problems. *SIAM/ASA J. Uncertain. Quantif.* **2024**, *12*, 723–758. [CrossRef]
23. Martin, N.; White, J.; Southard, P. A Null Space Sensitivity Analysis for Hydrological Data Assimilation with Ensemble Methods. *Hydrology* **2025**, *12*, 106. [CrossRef]
24. Banerjee, S.; Chattopadhyay, B. Multi-Stage Methods for Cost Controlled Data Compression Using Principal Component Analysis. *Mathematics* **2025**, *13*, 2140. [CrossRef]
25. Rosencwaig, A.; Gersho, A. Theory of the photoacoustic effect with solids. *J. Appl. Phys.* **1976**, *47*, 64–69. [CrossRef]
26. Bialkowski, S.E.; Astrath, N.G.C.; Proskurnin, M.A. *Photothermal Spectroscopy Methods*; John Wiley & Sons: Hoboken, NJ, USA, 2019.
27. Vargas, H.; Miranda, L.C.M. Photoacoustic and related photothermal techniques. *Phys. Rep.* **1988**, *161*, 43–101. [CrossRef]

28. Mandelis, A. *Principles and Perspectives of Photothermal and Photoacustic Phenomena*; Elsevier: Amsterdam, The Netherlands, 1992.
29. Galovic, S.P.; Soskic, Z.N.; Popovic, M.N.; Stojanovic, Z.; Cevizovic, D.; Stojanovic, Z. Theory of photoacoustic effect in media with thermal memory. *J. Appl. Phys.* **2014**, *116*, 024901. [CrossRef]
30. Nikolic, P.M.; Todorović, D.M. An investigation of semiconducting materials using a photoacoustic method. In *Technical Sciences Book 40, Monographs*; Serbian Academy of Sciences and Arts, Department of Technical Sciences: Belgrade, Serbia, 2001; p. DCXLVIII.
31. Perondi, L.F.; Miranda, L.C.M. Minimal-volume photoacoustic cell measurement of thermal diffusivity: Effect of the thermoelastic sample bending. *J. Appl. Phys.* **1987**, *62*, 2955–2959. [CrossRef]
32. Rabasovic, M.D.; Nikolic, M.G.; Dramicanin, M.D.; Franko, M.; Markushev, D.D. Low-cost, portable photoacoustic setup for solid samples. *Meas. Sci. Technol.* **2009**, *20*, 095902. [CrossRef]
33. Popovic, M.N.; Nesic, M.V.; Ciric-Kostic, S.; Zivanov, M.; Markushev, D.D.; Rabasovic, M.D.; Galovic, S.P. Helmholtz resonances in photoacoustic experiment with laser-sintered polyamide including thermal memory of samples. *Int. J. Thermophys.* **2016**, *37*, 116. [CrossRef]
34. Popovic, M.N. *Generalizovani Fotoakusticni odziv Dvoslojnih Struktura*; Zadužbina Andrejevíc: Beograd, Serbia, 2019. (In Serbian)
35. Jordović-Pavlović, M.; Raspopović-Milić, M.; Đorđević, K.; Nešić, M.; Popović, M. Using simulated data in computationally intelligent photoacoustics. *Eng. Today* **2023**, *2*, 25–37. [CrossRef]
36. Jordović-Pavlović, M.I.; Stanković, M.M.; Popović, M.N.; Ćojbašić, Ž.M.; Galović, S.P.; Markushev, D.D. The application of artificial neural networks in solid-state photoacoustics for the recognition of microphone response effects in the frequency domain. *J. Comput. Electron.* **2020**, *19*, 1268–1280. [CrossRef]
37. Djordjević KLj Markushev, D.K.; Popovic, M.N.; Nesic, M.V.; Galović, S.P.; Lukić, D.V.; Markushev, D.D. Photoacoustic Characterization of TiO2 Thin-Films Depositedon Silicon Substrate Using Neural Networks. *Materials* **2023**, *16*, 2865. [CrossRef] [PubMed]
38. Jordovic Pavlovic, M.I.; Markushev, D.D.; Kupusinac, A.D.; Djordjevic KLj Nesic, M.V.; Galovic, S.P.; Popovic, M.N. Deep Neural Network Application in the Phase-MatchCalibration of Gas–Microphone Photoacoustics. *Int. J. Thermophys.* **2020**, *41*, 73. [CrossRef]
39. Jordovic Pavlovic, M.; Raspopovic Milic, M.; Popovic, M.; Galovic, S.; Markushev, D. A method for efficient classification of microphones based on expert knowledge and computational intelligence. *Eng. Today* **2026**, *2*, 15–23. [CrossRef]


**Disclaimer/Publisher's Note:** The statements, opinions and data contained in all publications are solely those of the individual author(s) and contributor(s) and not of MDPI and/or the editor(s). MDPI and/or the editor(s) disclaim responsibility for any injury to people or property resulting from any ideas, methods, instructions or products referred to in the content.